SUPPLEMENTARY INFORMATION

Supplemental Information on Rupture Analyses

P and SH Wave Finite Fault Inversion

The body wave inversions yield predominantly bilateral slip, although there may be a slight asymmetry in the slip distribution with greater extent toward the northwest. The P- and SH-waveform matches for our preferred finite source model are shown in Fig. S3. The slip model accounts for about 78% of the weighted signal power in the 120-s-long interval used in the inversion, with the source time function representing slip during the first 60 s of rupture. The seismic moment was estimated as 2.5 x 10^{21} Nm (M_w 8.2), but experience indicates that this may be less reliable than a determination made at longer periods and we adopt a final moment of 1.8 x 10^{21} Nm (M_w 8.1) based on composite source modeling of 714-1000 s period Rayleigh waves. There are clearly some P wave motions about 100 s after the first arrival in the waveforms of stations in Asia (TATO, ENH, BJT) that are not matched by the source model. Using very long fault models extending toward the northwest allows the normal fault model to match this late energy, but as discussed below, the late signal appears to originate from a secondary event with different fault mechanism. The depth extent of rupture is not well resolved, but we find that localized regions of significant slip are present in all models extending to depths of 30-36 km (>24 km below the 6 km thick ocean layer). The likelihood that rupture during the mainshock extended this deep is strongly supported by the depth of the largest aftershock in the trench-slope region with a location and mechanism consistent with being on the mainshock rupture surface. This is the event of October 19, 2009 (22:49:37 UTC, 15.3°S, 172.2°W, M_w 5.9). The W-phase and GCMT solutions (Fig. 1) for this event have compatible normal fault geometries, with the W-phase centroid depth being 32.5 km. We inverted 40 azimuthally well-distributed teleseismic P waves for a finite source model for this event, assuming a hypocentral depth of 30 km. The resulting slip model and examples of fits to the data are shown in Fig. S4. The rupture centroid is confirmed to be about 32 km deep.

The rupture velocity of predominantly bilateral ruptures is usually not well resolved by teleseismic body wave data because their high apparent velocities provide limited resolution. Essentially, the slip distribution scales spatially directly with the assumed rupture velocity. However, surface waves have lower apparent velocities and are thus more sensitive to directivity effects. We compared observed and predicted of short-arc Rayleigh wave (R1) source time functions (discussed below) for many body wave models to bound the rupture velocity and spatial extent of the slip model. We compared predicted R1 STFs for the model in Fig. S2 with

azimuthally binned and stacked STF observations, finding little evidence for azimuthal variation of STF duration, consistent with a largely bilateral rupture. Preferred rupture velocities based on fitting the STF characteristics are less than 2 km/s, with the best fits being in the range 1-1.5 km/s. The model shown in Fig. S2 used 1.5 km/s.

Normal Fault Energy Estimation

Our quantification of the trench-slope failure favors rupture on a steeply dipping fault plunging toward the subduction zone, with faulting extending down to at least 24 km within the lithosphere. The finite-slip model in Fig. S2 was used to estimate the average slip properties of the normal faulting, with an average displacement of 10 m for the 3,510 km^2 of the fault surface with more subfault seismic moments greater than 10% of the peak subfault seismic moment. The static stress drop estimated for these well-resolved slip regions is 13 MPa. The short-period spectral levels for this event (Fig. S5) are higher than typical for interplate thrust events, and are consistent with a spectral model static stress drop of 5 MPa. The moderately high spectral amplitudes may account for strong shaking that triggered the widespread aftershock activity in the region. Using 33 teleseismic ground velocity recordings, an energy estimate[34] of 4.1 x 10^{16} J was obtained (assumed source P-velocity 7.3 km/s, S-velocity 4.1 km/s and density 3.1 g/cm^3). This is higher than an estimate of 2.8 x 10^{16} J from the USGS[11]. Using the preferred seismic moment for the normal faulting (1.8 x10^{21} Nm), estimated seismic energy/seismic moment ratios for this event range from 1.5 x 10^{-5} to 2.3 x 10^{-5}, which is typical of large intraplate ruptures (Fig. S5).

R1 Source Time Function Modeling

The R1 STFs were modeled using two- and three-source models, with the first source in each case involving radiation from the normal-faulting source and the later sources being thrust-faulting with mechanism constrained to be compatible with motion on the megathrust. A grid of possible secondary event locations was defined, and the amplitude and timing of thrust subevents were searched for by constructing synthetics for the STFs and comparing them with the data. The results for the best fitting model are shown in Fig. 2, with the search parameter results shown in Fig. S6. These results support the occurrence of two major thrust events about 60 and 96 s after the centroid of the normal faulting, at locations of 15.5°S, 172.5°W, and 16.0°S, 172.5°W. The second thrust location and the differential time between events is very close to that estimated from regional surface wave modeling described below.

To explore the reliability of the regional waveform modeling with a few stations, we performed a grid-search to map out the range of three subevent models that were consistent with the observed R1 STFs. We selected 43 STFs that fit the convolutional model with less than 5% misfit and that had a balanced azimuthal distribution. We tracked both L2 and L1 misfits but equalized the overall amplitude of the observed and predicted signals before computing the misfits. Visual inspection of the fits for the best model indicates that the amplitudes of most signals are well matched. A few waveforms are poorly matched but most of these correspond to directions where we have few observations and cannot correlate features from signal-to-signal. The L1 and L2 fits for the signals favor the same solutions, so we believe that these few outliers do not systematically affecting the solution.

We fixed the normal faulting onset to match the USGS epicenter. Preliminary calculations using just a normal fault parameterized with a symmetric triangle suggested that the initial pulse of the observed STFs were fit well with a duration of 64 s. We held this value constant during the search. The normal fault moment and the combined moment of the two thrust events were held constant (1.8×10^{21} for the normal faulting event, 1.05×10^{21} N-m for the two thrusts combined). Based on the regional waveform modeling, we held the ratio of the thrust events to be roughly comparable, and checked that assumption after the fact using the optimal locations). Not surprisingly, using the optimal locations and time shifts favor the roughly equal moments for the two events, demonstrating that the result is at least stable with respect to that assumption. We also fixed the duration of the two thrusts to 20 s. With little sensitivity to depth, we fixed the depth of all the sources at 15 km. In all, we tested just over 15,000 candidate three-event models, varying only properties of the two thrusts.

We performed the location search over centroid grid with a spacing of 0.25°. We constrained the first thrust location latitude to be between -15.75° and -16.25° and longitude to lie between -172.25° and -172.75°. The second thrust position was allowed to vary more in the latitude range -15° to -17° and the longitude range -172.0° to -173.5°. The resulting models indicate a north-to-south rupture with only a few 10's of kilometers shift in the centroid locations of the two thrusts. The first thrusting event delay (relative to the normal faulting event) was tested with values of 36, 48, and 60 s, and the second subevent range was tested with values of 64, 72, 80, 88, 96, and 104 s.

The best fitting solution has a thrust subevent at 60 s with a location at -15.75° -172.25°, and a second thrust subevent 36 s later, at a location of -16.0°, -172.25°. Solutions that fit nearly as well included a secondary source that was co-located with the first event, or located as far as

50 km to the south. Other reasonably well-fitting solutions shifted the source slight to the south and west. The time delays remained the same for all the best- fitting candidate solutions.

Back-Projections of Teleseismic P waves from Regional Networks

The back-projections from all six networks are shown in Supplementary Movie 1. The network geometries are shown in the first frame of the animation. Owing to the different apertures, slightly different frequency bands were used in the imaging. A four-pole Butterworth bandpass filter was applied with the following corner frequencies: 0.2-1.0 Hz (Australia, East Asia), 1.0-3.0 Hz (F-Net, Hi-Net, Alaska), and 0.5-2.0 Hz (USArray). The corresponding array response functions[35] are shown alongside the station maps. Normalized beam power (as a function of space and time) is shown in the animation. The images show a trench-slope rupture that initially appears to extend toward the northwest, but there is late energy (50-70 s) originating to the southeast of the epicenter, consistent with bilateral rupture. In the time period of about 50-120 s weak secondary energy appears to originate on or above the Tonga megathrust, with arrays at different azimuths showing this more or less clearly depending on the resolution and pattern of the artifacts. Variations among the animations are primarily created by variations in the sampling of the focal sphere and differing levels of coherency across the arrays. For the F-Net array in Japan, selected frames are shown in Fig. 3, at delays of 25, 52, 91, and 118 s.

These highlight the radiation from the trench-slope, which dominates for the first 60 s, and the spatially offset bursts of coherent short-period energy from triggered activity on or above the megathrust to the southwest. To confirm that these features are not artifacts of the array geometry, we computed 73 synthetic seismograms for the F-Net stations using the finite-source model for the trench-slope normal faulting and back-projected them in the same fashion as the data. Shapshots from the back-projection of synthetics for the same times as in Fig. 3 are shown in Fig. S7. No artifacts are seen on the megathrust, confirming that the features in the data are caused by distinct sources.

Free oscillations

As additional confirmation of the total thrust moment, we predicted observed toroidal and spheroidal free oscillation spectra computed for the available time interval prior to a large earthquake in Vanuatu on September 30 at the azimuths where normal fault radiation predicted weak motion (Fig. S14). The predictions were based on computing normal mode ground motions for the W-phase and composite 3-source models, processing the signals in the same fashion as the data. Comparisons of the spectra indicate that the composite model accounts well

for the enhanced toroidal motions for stations in Asia (e.g., MAJO in Fig. S14) and North America (e.g., TUC in Fig. S14) which are poorly matched by the W-phase solution, as well as accounting for the decrease in spheroidal mode amplitudes at very long periods due to destructive interference between the normal and thrust fault radiation (e.g., CAN Z in Fig. S14).

Strong Motions

One available strong-motion record at station AFI (epicentral distance 1.7° from the normal-faulting hypocenter) was inspected, showing evidence for extended shaking caused by the combined normal and thrust faulting (Fig. S15). Significant ground acceleration continued for over two minutes, with the envelopes of the three-component motions indicating modulation of the S wave signals with packets in the time intervals 50-80 s, 80-100 s, and 110-130 s. The secondary thrust events are at larger distance from the station than the normal faulting but there is evidently some short-period signal associated with the triggered activity.

Meaning of a Point-Source Solution for a Multiple Source Composite Event

The total moment of the normal faulting event appears to be about twice the combined moment of the thrust faulting subevents in the main episode of the Samoa-Tonga great earthquake doublet. Fig. S16 shows the focal mechanisms and relative source strengths of the three subevents. The question then arises as to what is the meaning of a point-source representation of the combined seismic radiation from these events, as characterized by long-period wave analyses like the W-phase and GCMT procedures? The simplest moment tensor of the composite source is one that simply computes the tensor sum of the individual moment tensors, ignoring time differences:

$$M_c = \Sigma M_i$$

In this case of adding normal and thrust faults together, there is substantial cancellation of seismic moment value, which does not accurately characterize the shorter-period shaking. A definition that allows for the time variation between the subevents is:

$$M_c(t) = \sum M_i(t - t_{di})$$

In the frequency domain this is:

$$\hat{M}_c(\omega) = \sum \hat{M}_i(\omega) e^{-i\omega t_{di}}$$

This indicates a frequency-dependent moment tensor, for which each element has a different delay. Computation of time-dependent moment tensors is viable, but it can be difficult to interpret the resulting functions. One can alternatively seek to represent the moment tensor for the composite event in the form:

$$\hat{M}_{c0}(\omega)e^{-i\omega t_d} \approx \sum \hat{M}_i(\omega)e^{-i\omega t_{di}}$$

Where $M_{c0}(\omega)$ is the moment tensor of the composite event with real elements, and t_d is a common time delay for all of the elements. Solving in a least-squares sense for the moment and delay for a given frequency, examples of the effective moment tensor for the composite 3-source model for varying periods are shown in Fig. S16. In the period range 200-500 s, the composite model closely resembles the W-phase solution (Fig. 1), as expected. Near 200 s, the moment tensor is not the same as the GCMT solution (Fig. 1), which might be a result of the specific sensitivity of the waveform inversion to the interfering ground motions.

Supplementary References

34. Venkataraman, A. & Kanamori, H. Observational constraints on the fracture energy of subduction zone earthquakes. J. Geophys. Res. **109**, 10.1029/2003JB002549 (2004).

35. Xu, Y., Koper, K. D., Sufri, O., Zhu, L. & Hutko, A. R. Rupture imaging of the M_w 7.9 12 May 2008 Wenchuan earthquake from back projection of teleseismic P waves. *Geochem. Geophys. Geosys.* **10**, Q04006, doi:10.1029/2008GC002335 (2009).

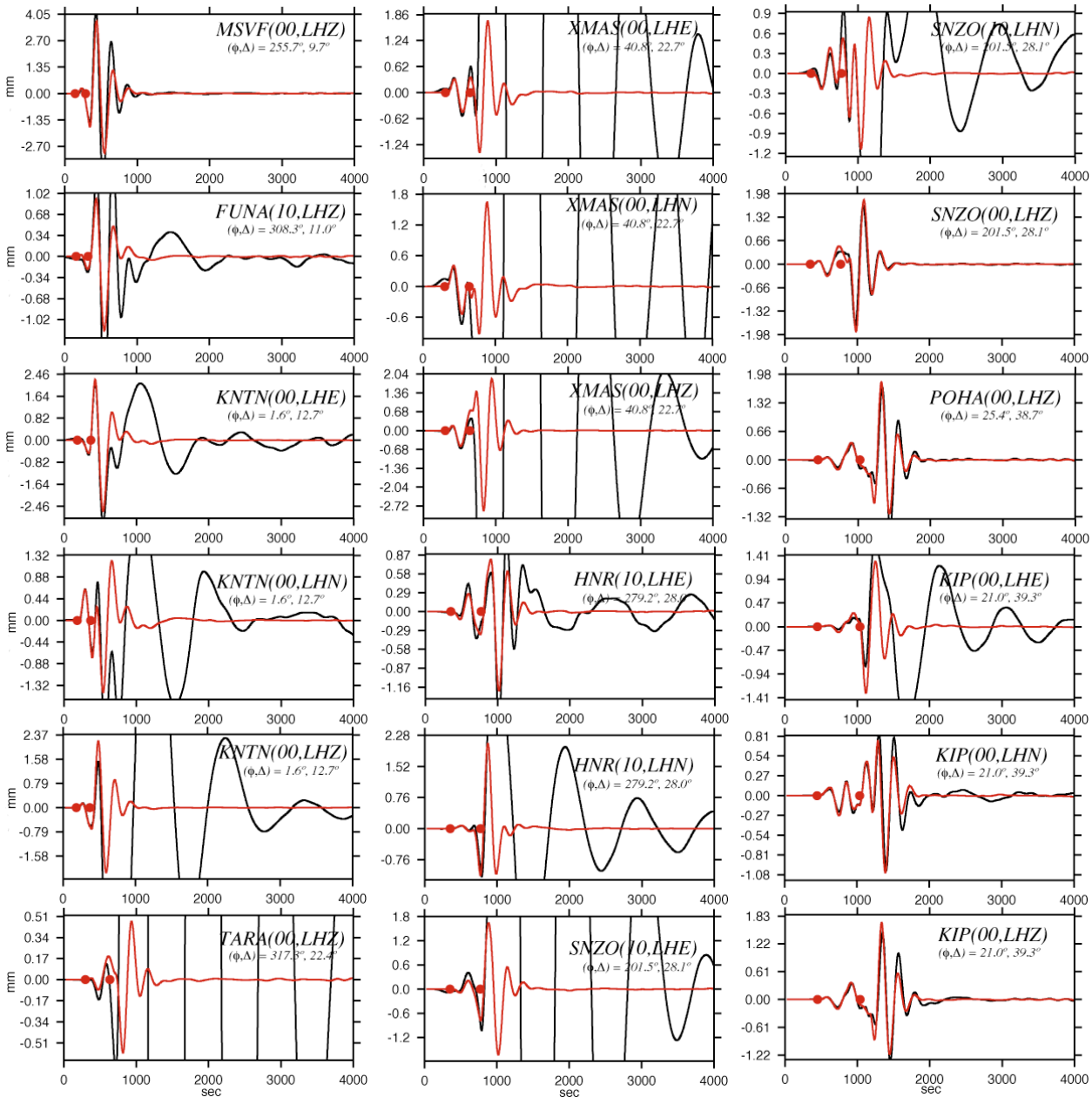

Figure S1. Examples of observed (black lines) and predicted (red) lines for the W-phase inversion for global stations at varying azimuth (ϕ) and distance (Δ). The passband is 200 to 1000 s. The W-phase time window is indicated by the two red dots. Many of the closer distance stations go off-scale (non-linear) when the strong surface waves arrive, but the W-phase portion of the signal is still useable.

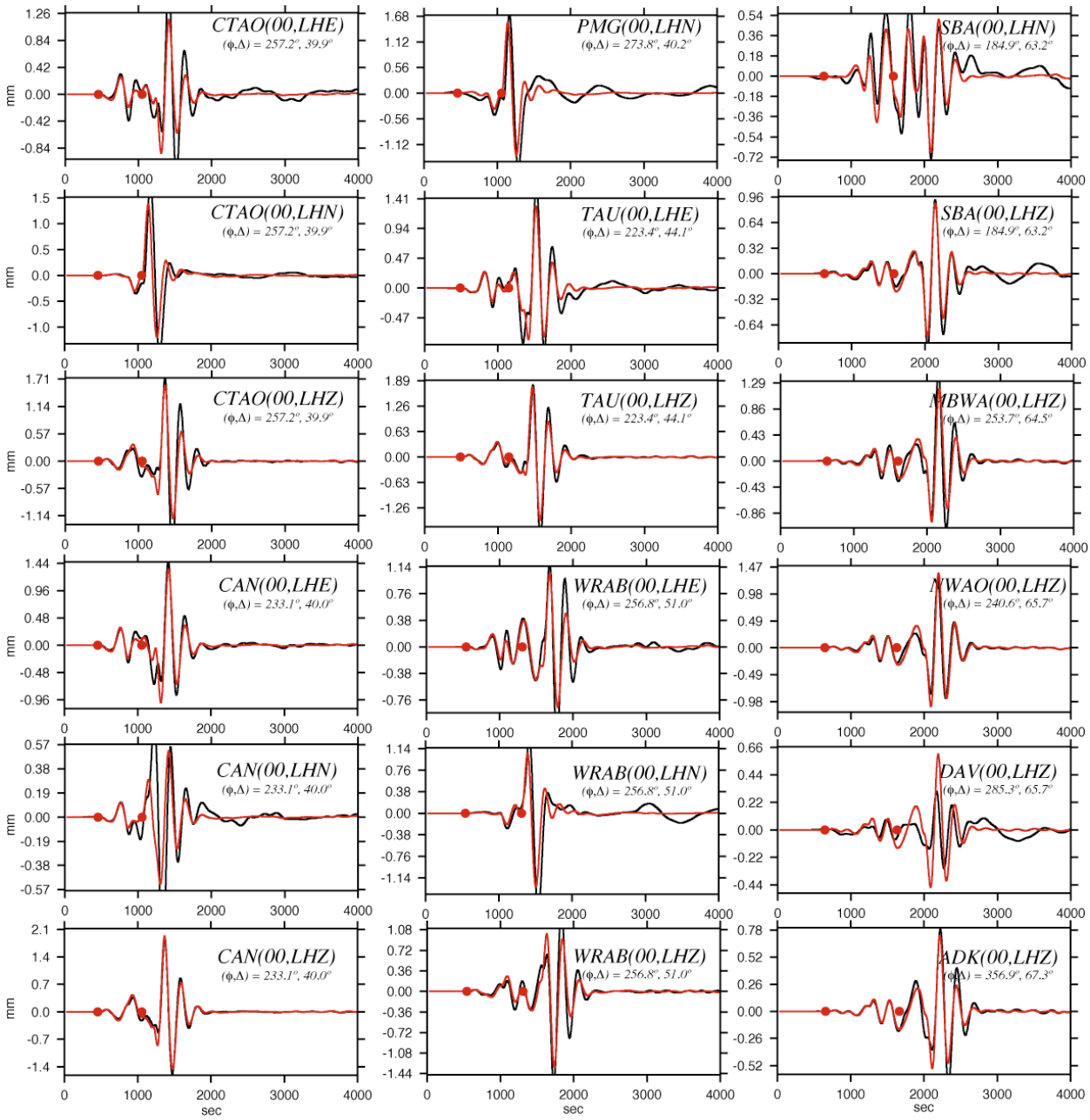

Figure S1. Continued.

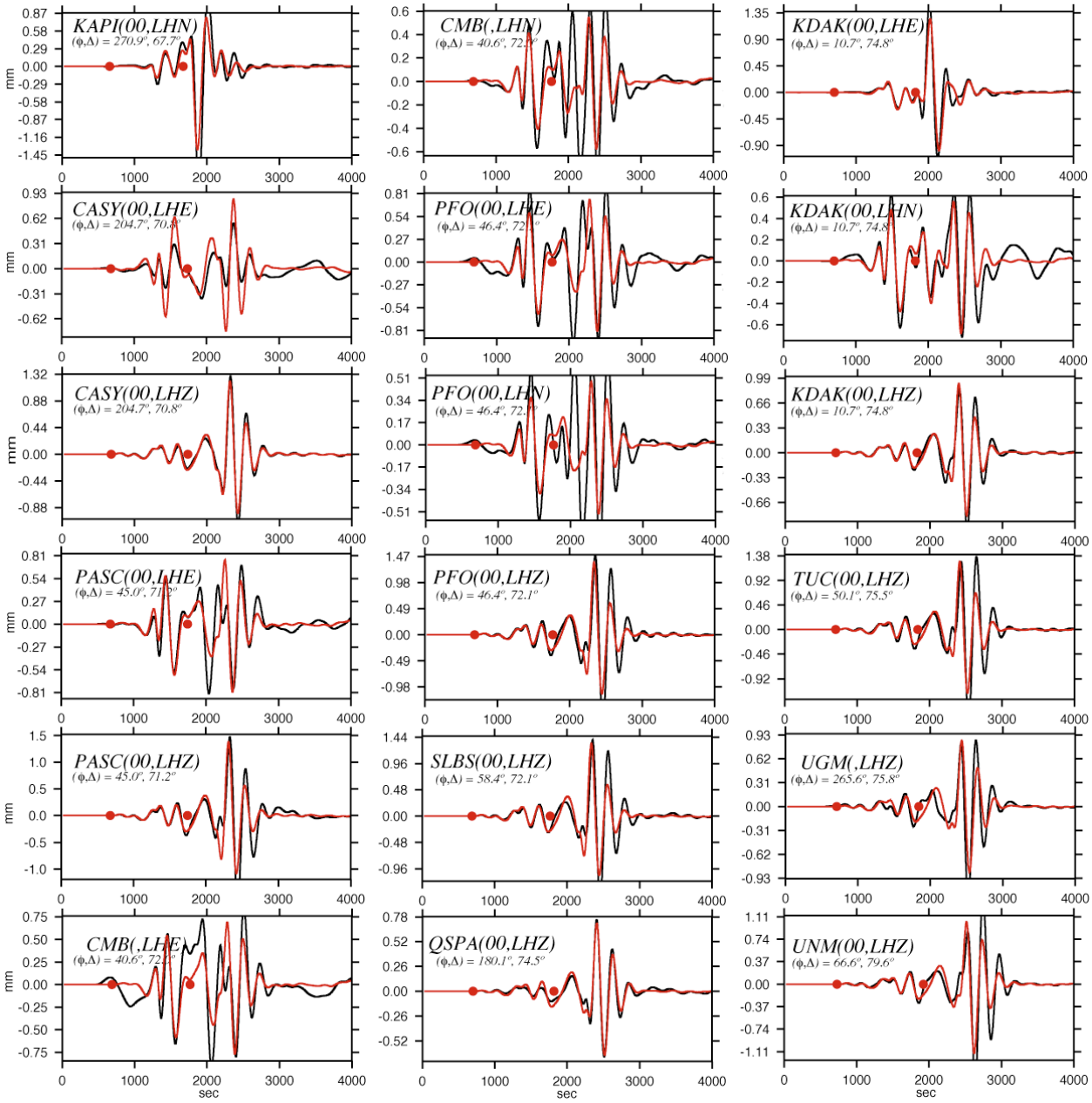

Figure S1. Finished.

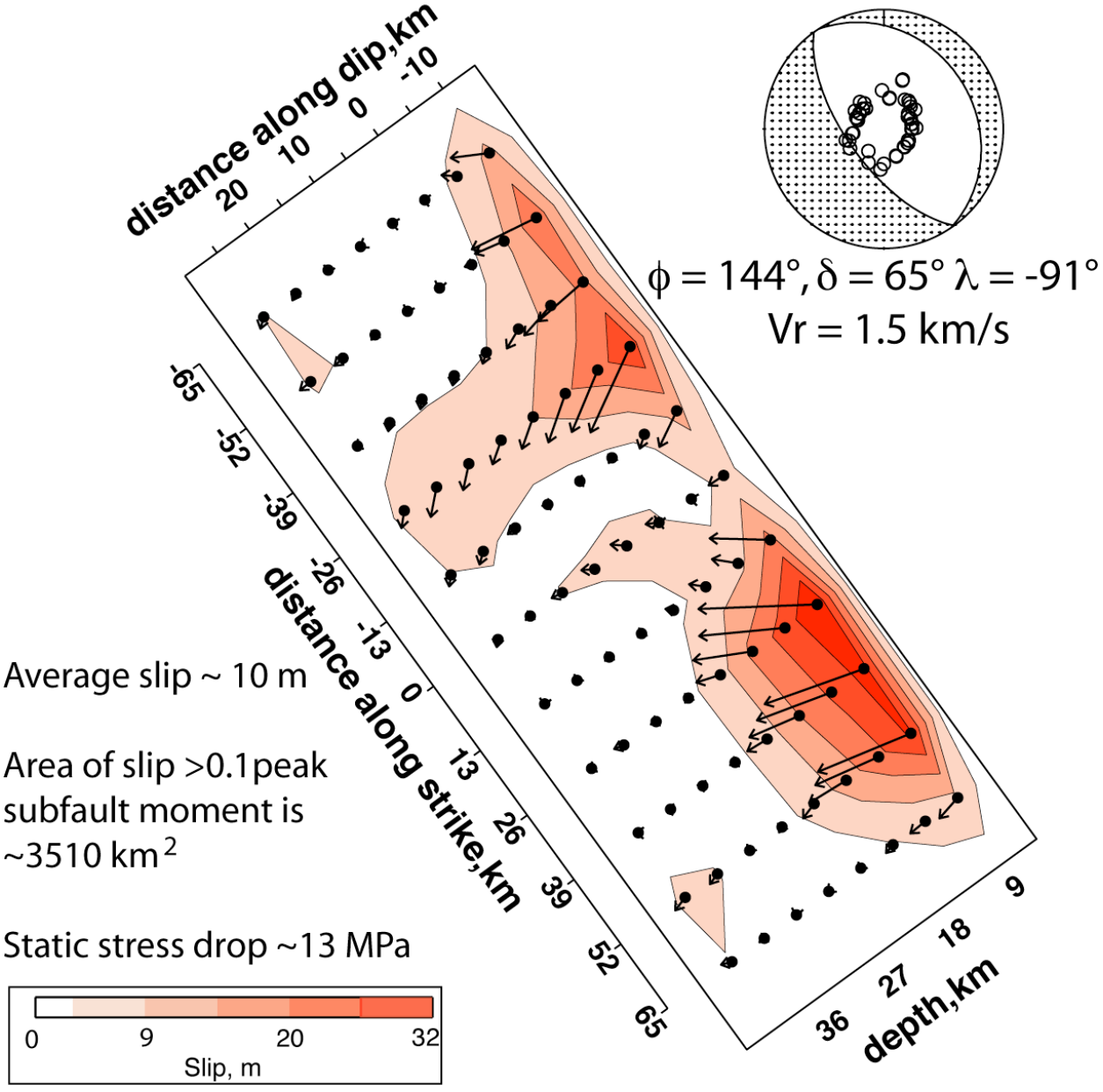

Figure S2. Finite source rupture model for the normal faulting component of the Samoa-Tonga great earthquake triggered doublet. The gridded distribution of slip on the fault plane steeply dipping toward the southwest from the focal mechanism on the upper right, with strike ϕ = 144°, and dip δ = 65°, is shown with colors contouring the average slip in m, with the vectors indicating the direction of slip of the hanging wall (upper) side of the fault relative to the foot wall. The inversion used teleseismic P and SH waves with the distribution indicated by the circles in the focal mechanism. Waveform fits are shown in Fig. S3. The rupture velocity, V_r is 1.5 km/s. The grid origin (0, 0) is located at the USGS location in the trench-slope shown in Fig. 1. The average rigidity is 5.1 GPa, and the seismic moment is 1.8 x 10^{21} Nm.

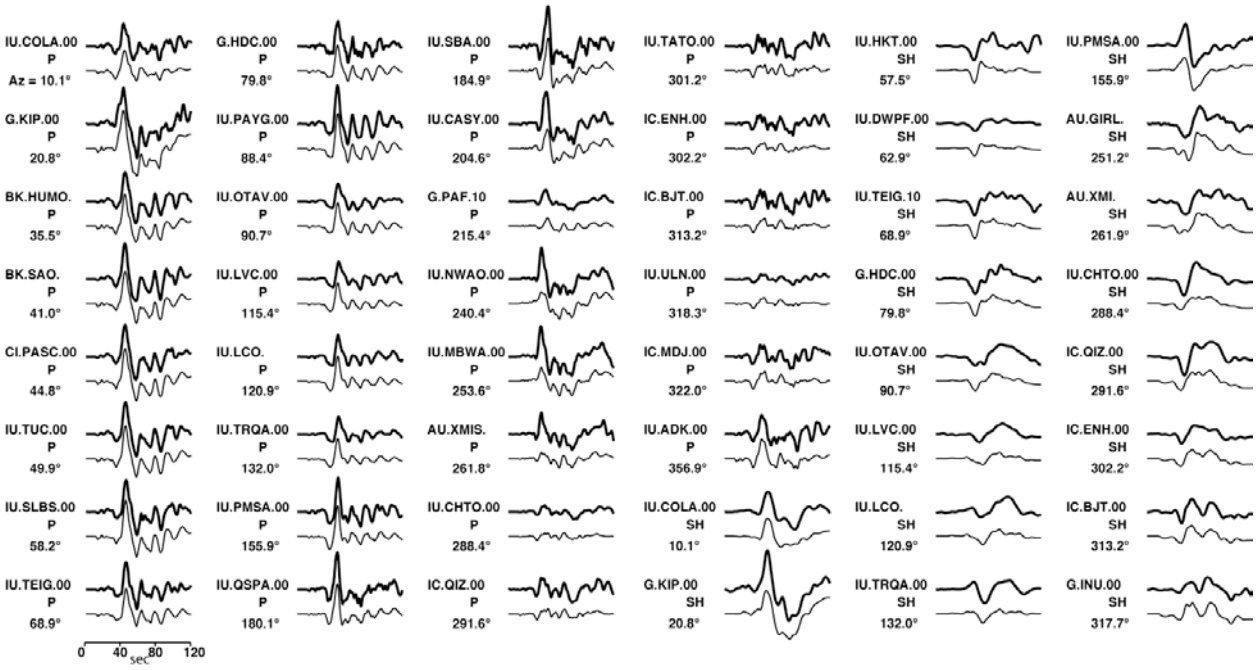

Figure S3. Comparison of observed (upper bold traces) and computed (lower light traces) P and SH wave ground displacements for the 29 September 2009 Samoa earthquake. The data were obtained from globally distributed seismic stations with the indicated station names at varying azimuths (Az) from the source region in the epicentral distance range 30°-100°. The computed traces are for the finite-source slip model in Fig. S2. The signals have true relative amplitude scales except that all SH traces are plotted at 1/5 amplitude relative to the P waves.

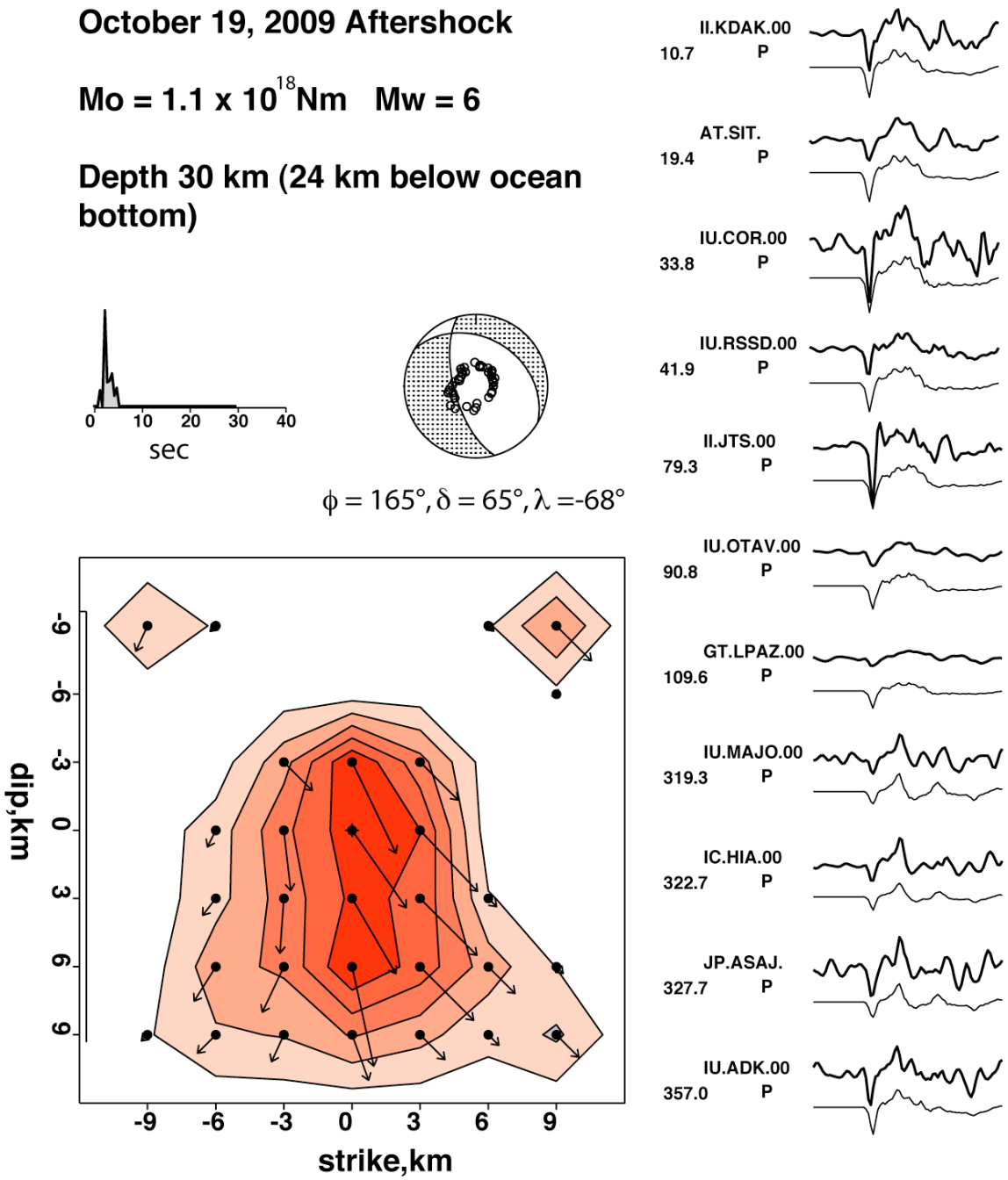

Figure S4. Finite-fault rupture model for the October 19, 2009 normal faulting aftershock. The fault geometry is assumed to be the same as for the mainshock, and is close to the GCMT and W-phase solutions for this event. The centroid depth was assumed to be 30 km for this model, with the fit to some of the 40 teleseismic P-waves at the indicated azimuths being shown on the right (observed are bold lines, synthetics are thin lines).

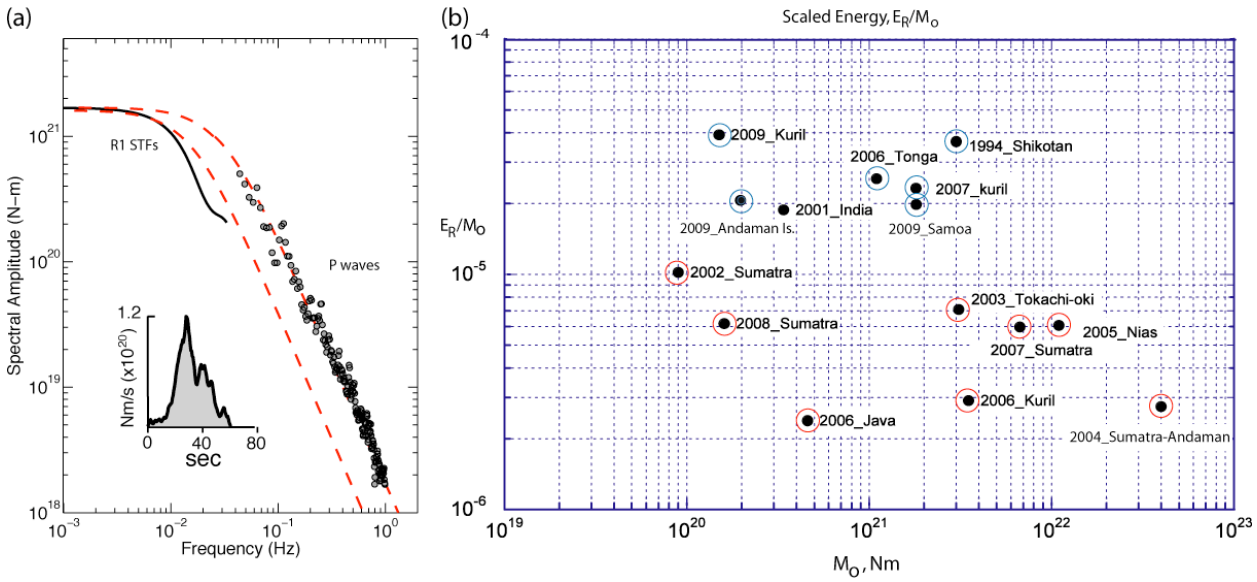

Figure S5. Source attributes of the normal faulting. (a) The source spectral amplitude obtained from analysis of Rayleigh waves (solid black line) and the geometrical average of 33 teleseismic P-wave ground velocity spectra (points), with superimposed theoretical spectra (red dashed curves) for static stress drops of 1 MPa (left curve) and 5 MPa (right curve). The inset shows the source function time history of the normal faulting rupture, obtained from inversion of P and SH waves. (b) Seismic-moment-scaled seismic energy measures for recent large intraplate slab (blue circles, and the non-slab 2001 India event) and interplate (red circles) earthquakes. The 2009 Samoa event plots close to the 2007 Kuril trench-slope event, sharing a tendency for high scaled energy with other intraplate ruptures.

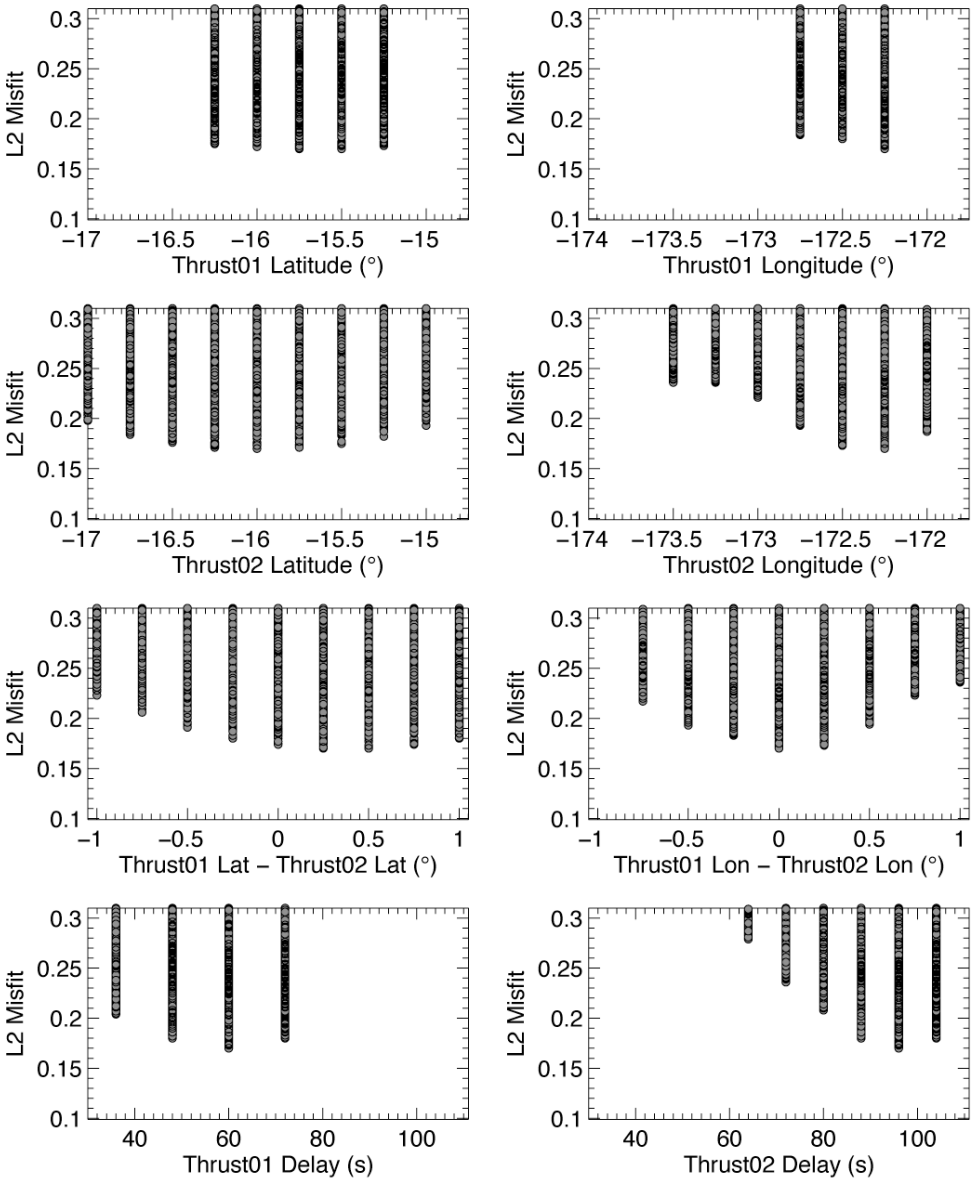

Figure S6. Summary of R1 STF parameter search for location and timing of the two secondary thrust events. Least-squares (L2) misfits are shown for 15,000 model parameter combinations. The models with lowest misfit are similar for L1 and L2 norms of the amplitude normalized comparisons of data and synthetics.

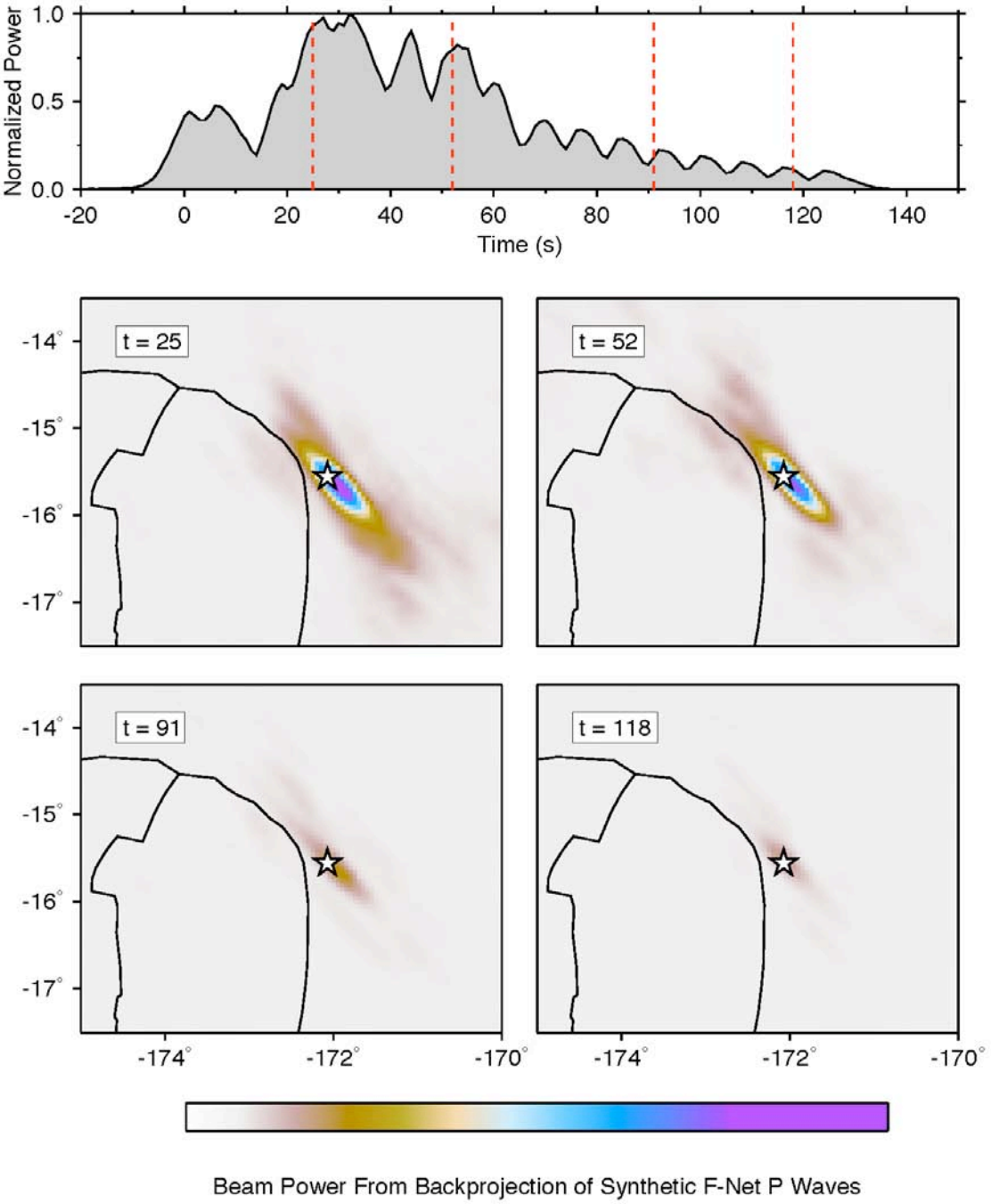

Figure S7. Snapshots for the back-projection of synthetic seismograms for the finite-source model in Fig. S2 for 73 stations of the Japanese F-Net. These correspond to the snapshots shown for the actual data in Fig. 3. There are no artifacts apparent in the Tonga Block, indicating that the array geometry suitably localizes the energy radiated from the outer trench slope event. The appearance of features along the megathrust in the data back-projection supports the interpretation of triggered activity.

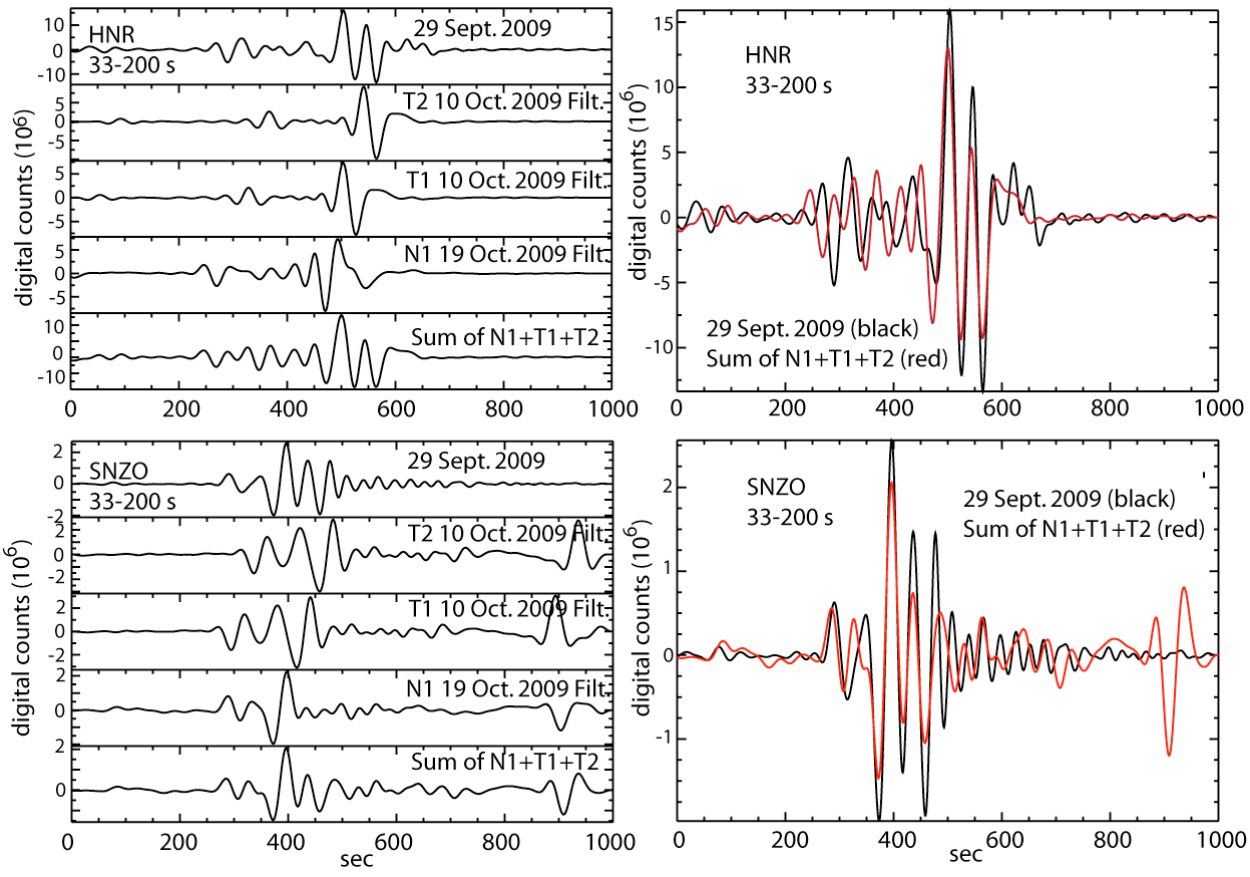

Figure S8. Modeling of regional R1 (HNR) and G1 (SNZO) phases using empirical Green's functions. The observations from the 29 September 2009 sequence are modeled by shifting and summing source-time function filtered recordings at the same stations from the 19 October 2009 normal faulting aftershock (N1) and the 10 October 2009 thrust faulting aftershock (T1, T2). The source time function for N1 was taken from the finite-fault inversion, while 20-sec rise time, 20-sec fall triangle functions were used for T1 and T2. The waveform fitting was done for the 50 to 200 s pass band. These traces are the corresponding predictions for the 33 to 200 s pass band. The observed (black) and predicted (red) waveforms for each station are superimposed on the right.

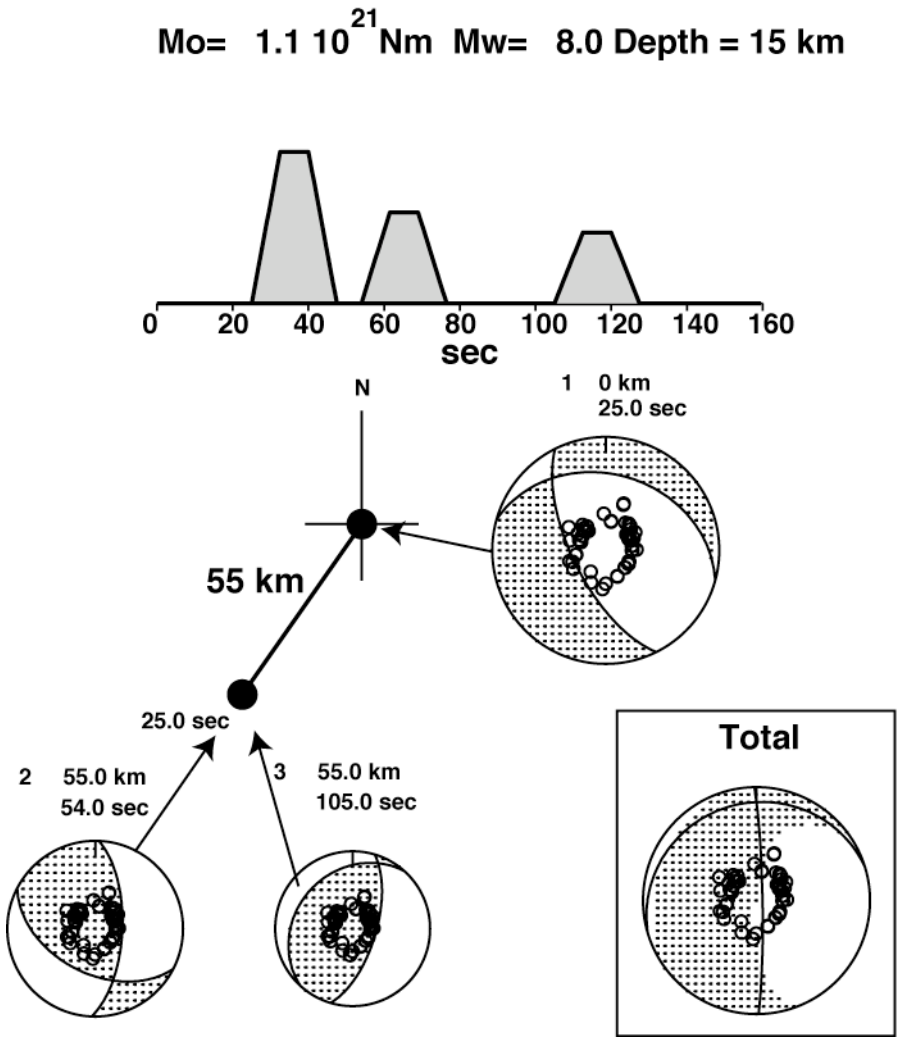

Figure S9. Variable fault geometry iterative inversion of teleseismic P and SH waves. The same data set used in the finite-fault inversion for the normal faulting component (Fig. S3) was used, seeking a parsimonious model with three subevents that could either be at the normal fault hypocenter or located 55 km to the SW on the megathrust location indicated by regional R1 and G1 modeling. The inversion returned a large normal fault subevent consistent in geometry with the finite-source model, and two secondary thrust fault subevents at 54 and 105 s which were located at the megathrust position option. Trapezoidal source functions with 7.5 s rise, 7.5 s flat and 7.5 s fall were assumed. The inversion is not robust for details of the focal mechanisms, but does indicate the consistency of the teleseismic P and SH signals with secondary thrusting. The direct sum of the moment tensors gives the total mechanism shown in the box; this is similar to the W-phase solution.

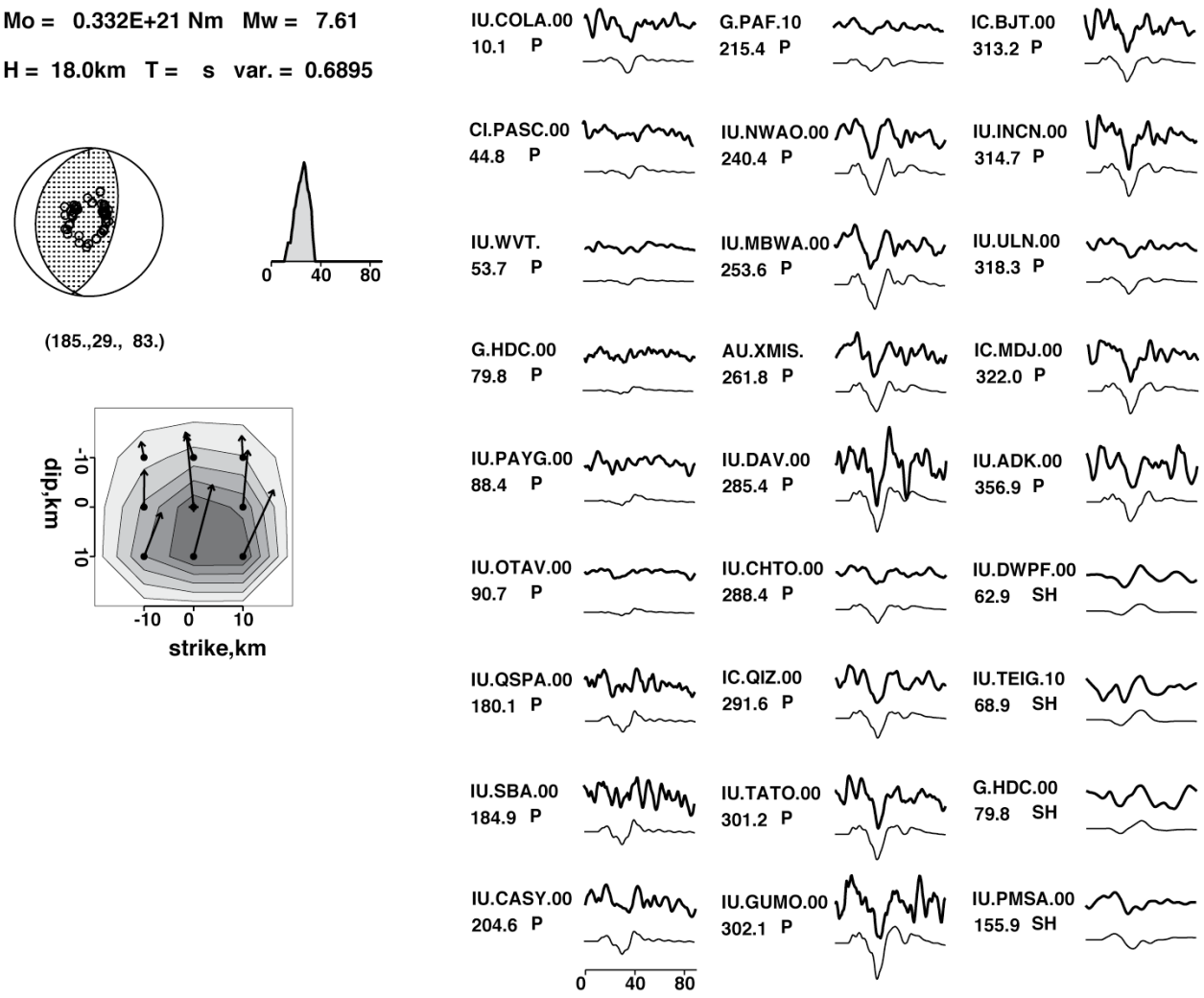

Figure S10. Inversion for the second thrust fault event radiation from the megathrust, assuming the tectonically defined fault geometry (focal mechanism with strike $\phi = 185°$, dip $\delta = 29°$. The same 48 P and SH wave signals as used to model the normal fault radiation (Fig. S3) were inverted, after shifting the onset times by 90 s plus corrections for spatial offset of the source to the west. Half of the data are shown here, with their azimuths being indicated below the station names. All amplitudes are on true relative scale, but with the SH waves reduced by a factor of 5. The source time function of each grid point was parameterized by 5 3-s rise, 3-s fall triangles, and a hypocentral depth of 18 km was assumed. The noise levels are high due to coda from the earlier normal and thrust faulting, but the relative strengths of the P waves are well matched by the thrust geometry.

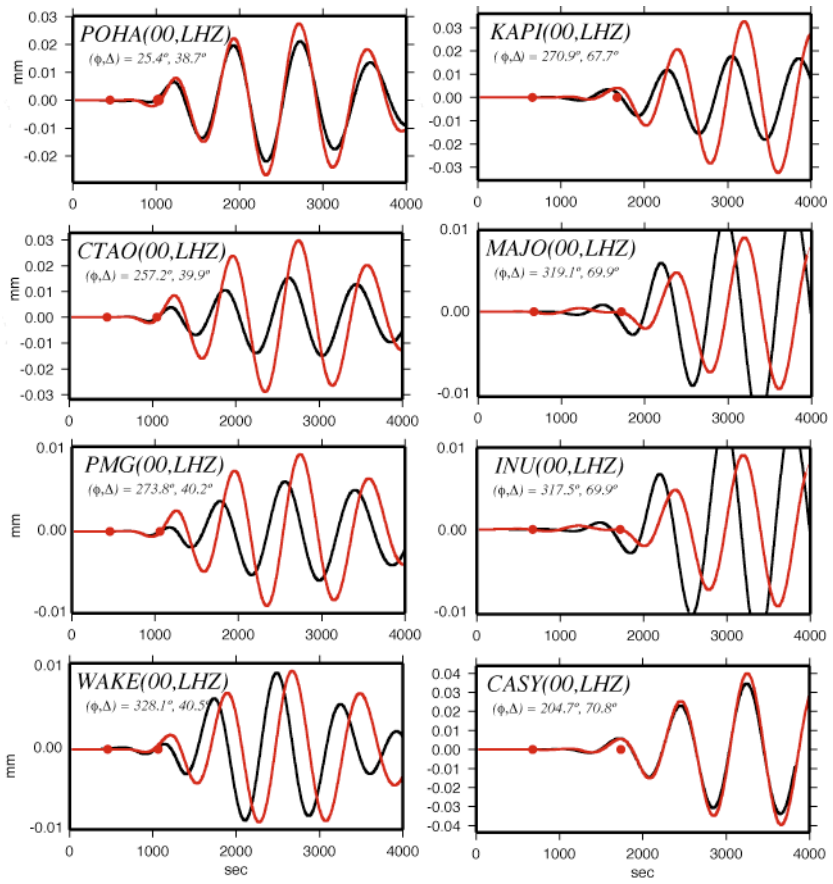

Figure S11. Predictions of the observed ultra long-period Rayleigh wave ground motions (black) in the period range 774-1000 s for the W-phase point-source solution (red). At these periods, the radiation senses the sum of the three events, so matching the phase is particularly important. The maps indicate the azimuth and distance of the station from the source. The red dots on the traces indicate the W-phase interval. Note the poor phase agreement for many of the stations.

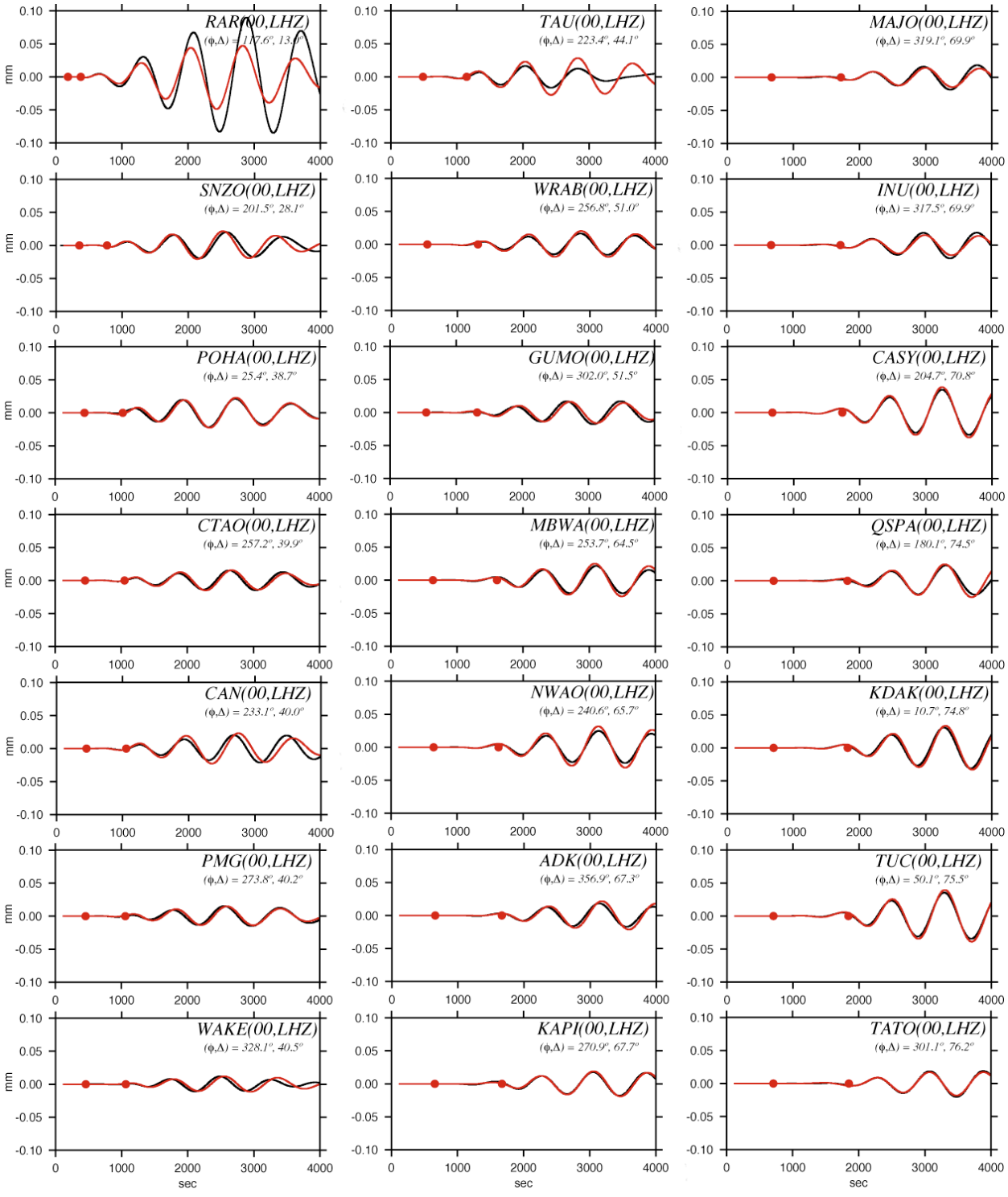

Figure S12. Predictions of the observed ultra long-period Rayleigh wave ground motions (black) in the period range 774-1000 s for the composite three-event source model (red). At these periods, the radiation senses the sum of the three events, so matching the phase is particularly important. The maps indicate the azimuth and distance of the station from the source. The red dots on the traces indicate the W-phase interval.

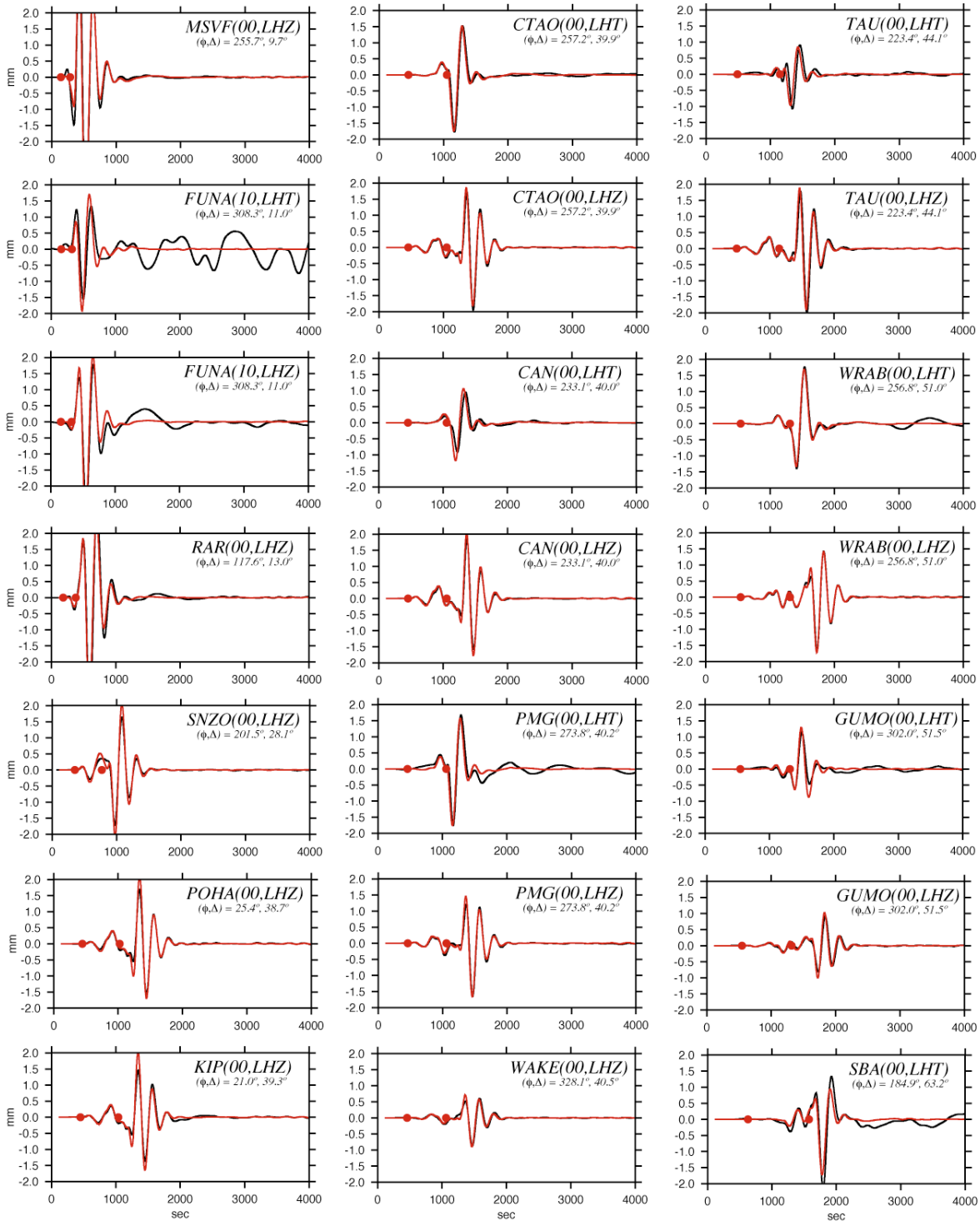

Figure S13. Predictions of the observed Love (LHT) and Rayleigh wave (LHZ) ground motions (black) in the period range 200-1000 s for the composite three-event source model (red). The waveforms are sensitive to the relative timing and focal mechanisms of the normal and thrust event radiation. The maps indicate the azimuth and distance of the station from the source. The red dots on the traces indicate the W-phase interval.

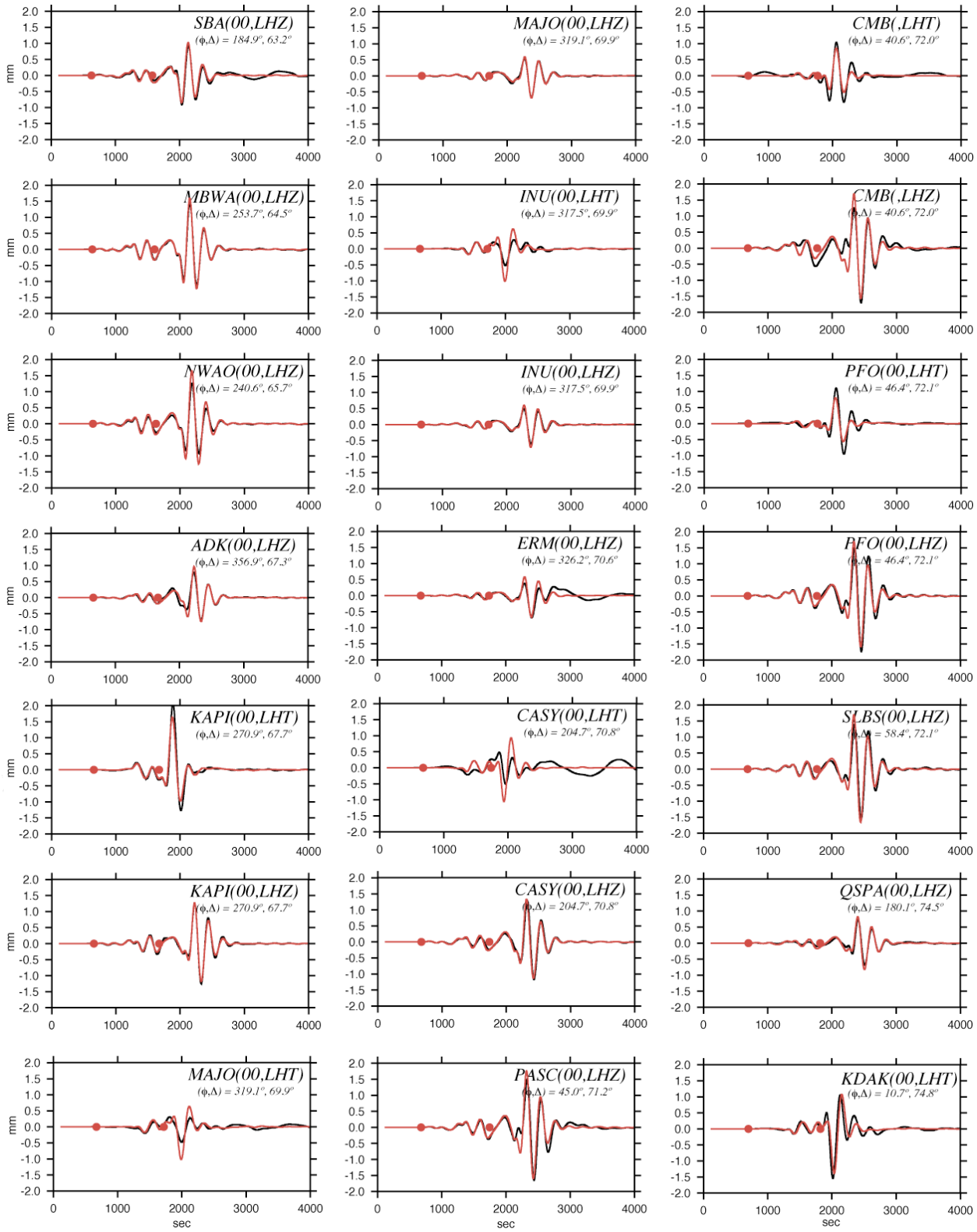

Figure S13. Continued.

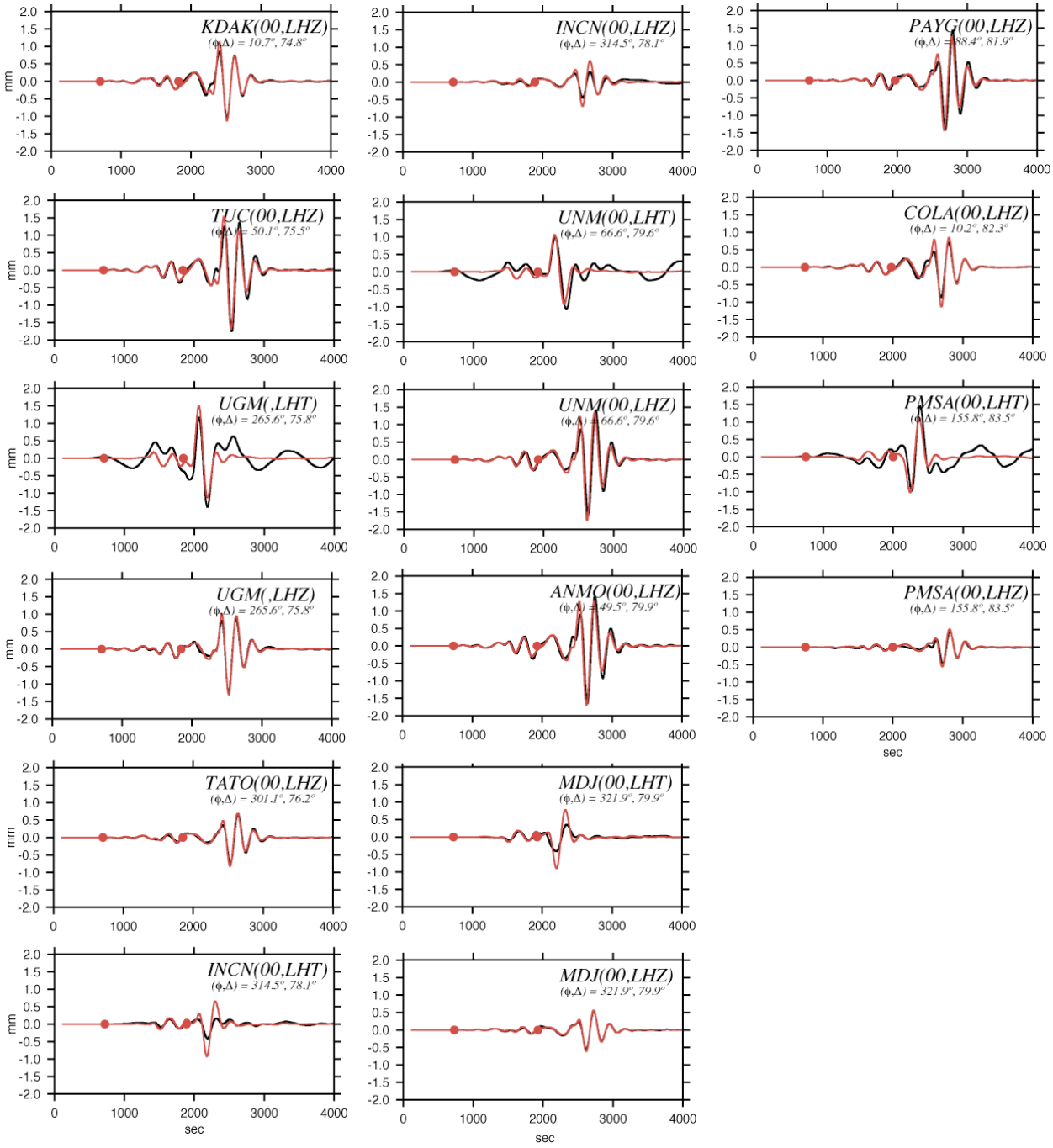

Figure S13. Finished

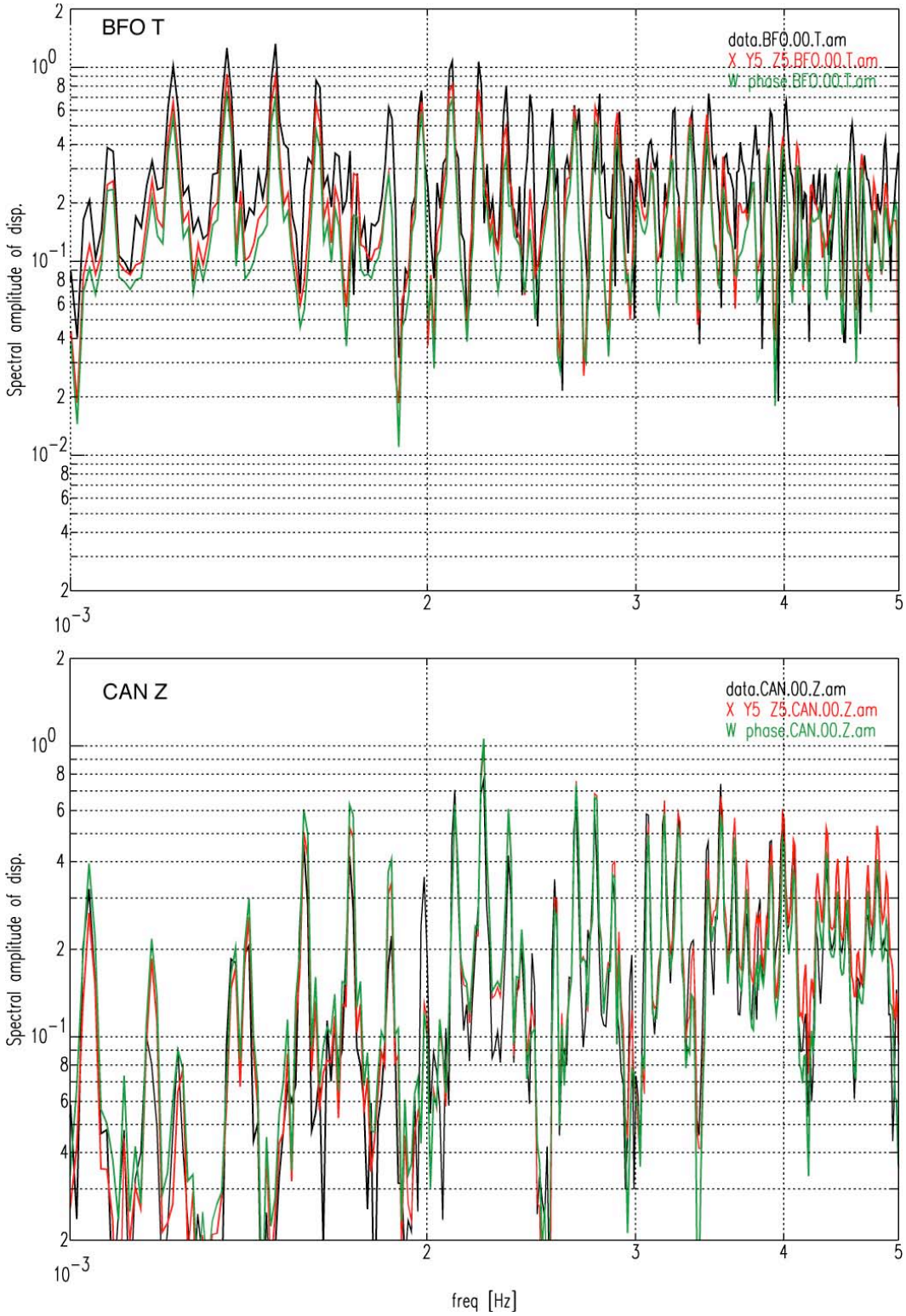

Figure S14. Toroidal (T) and spheroidal (Z) mode spectra for global stations (black) compared with predictions for the W-phase (green) and 3-Source (red) models. At stations MAJO, NWAO and TUC the ground motions expected for the normal faulting component are small, and the addition of the thrust radiation greatly improves the toroidal mode excitation levels.

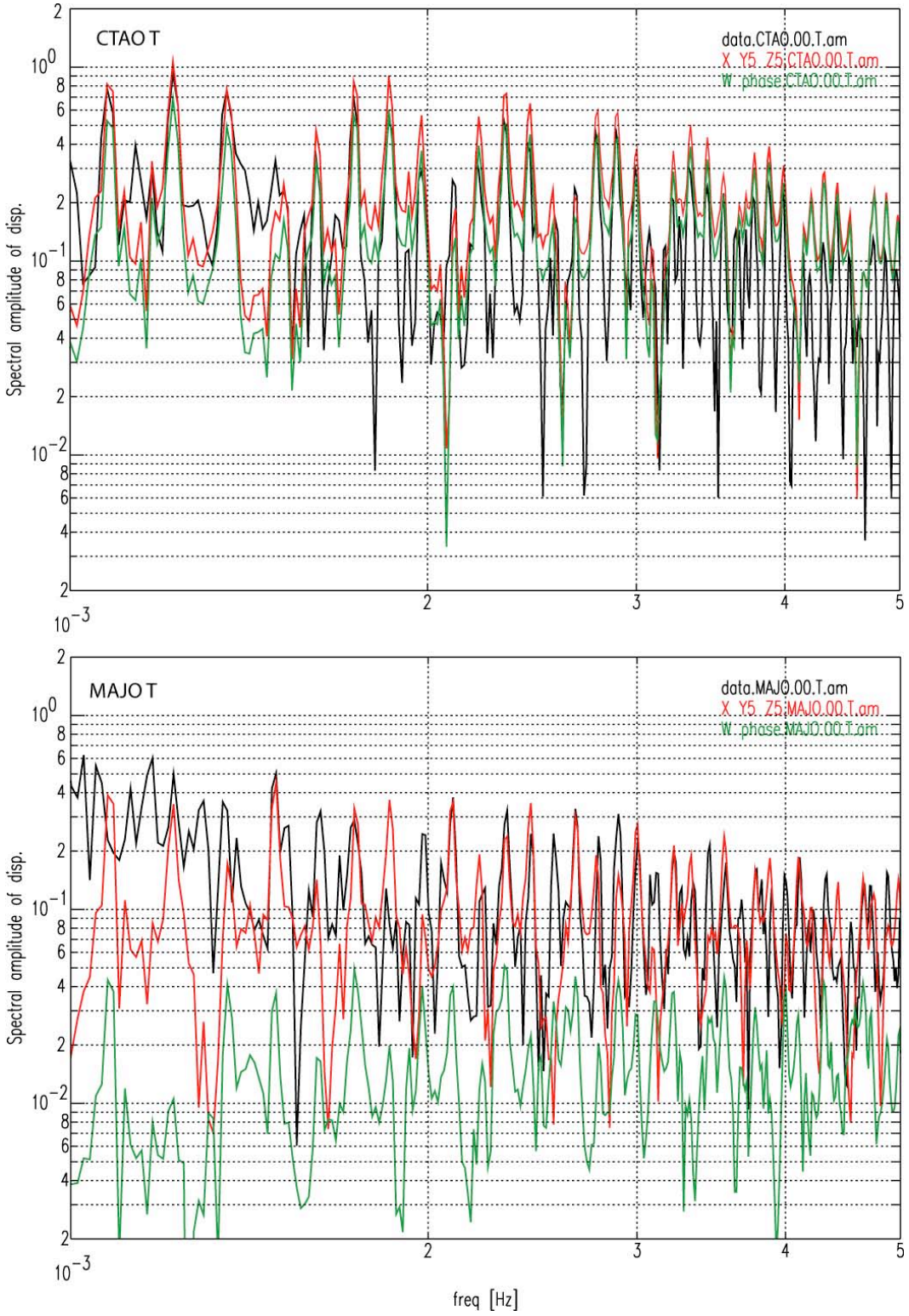

Figure S14. Continued.

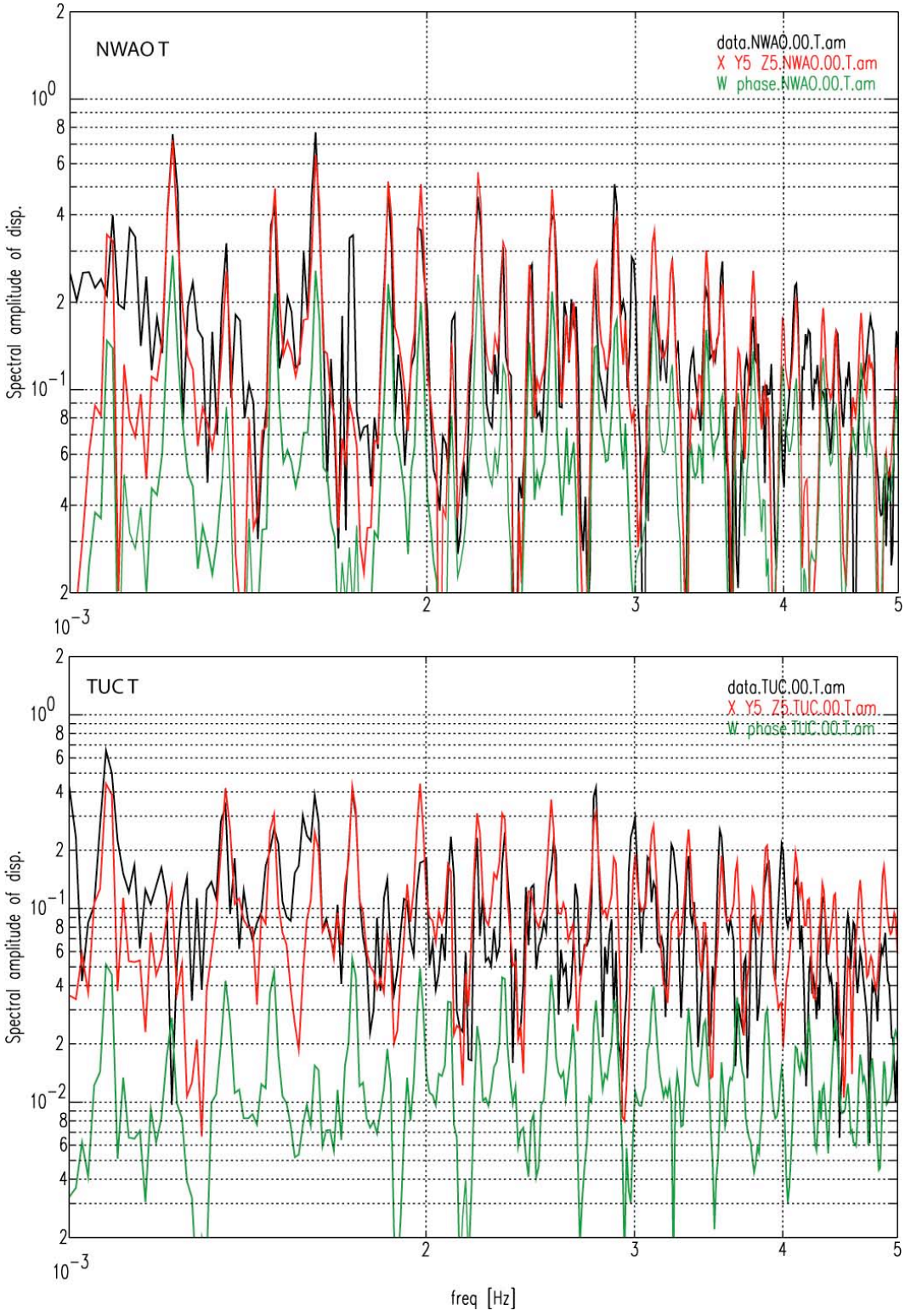

Figure S14. Finished.

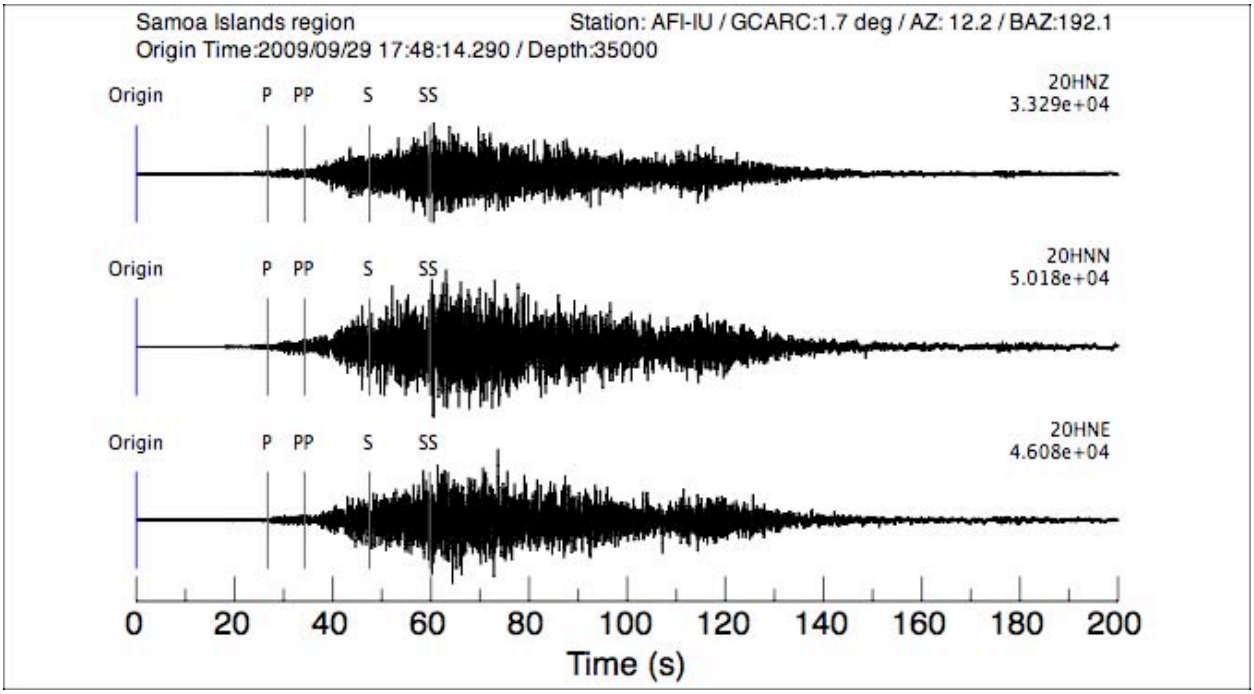

Figure S15. Three-component strong-motion record at AFI, showing the extended duration of high frequency shaking. In our composite model, the shaking is primarily caused by S energy from the trench-slope event up to about 80 s, with contributions from the first thrust event from 70 to 100 s and from the second thrust from 110 to 130 s.

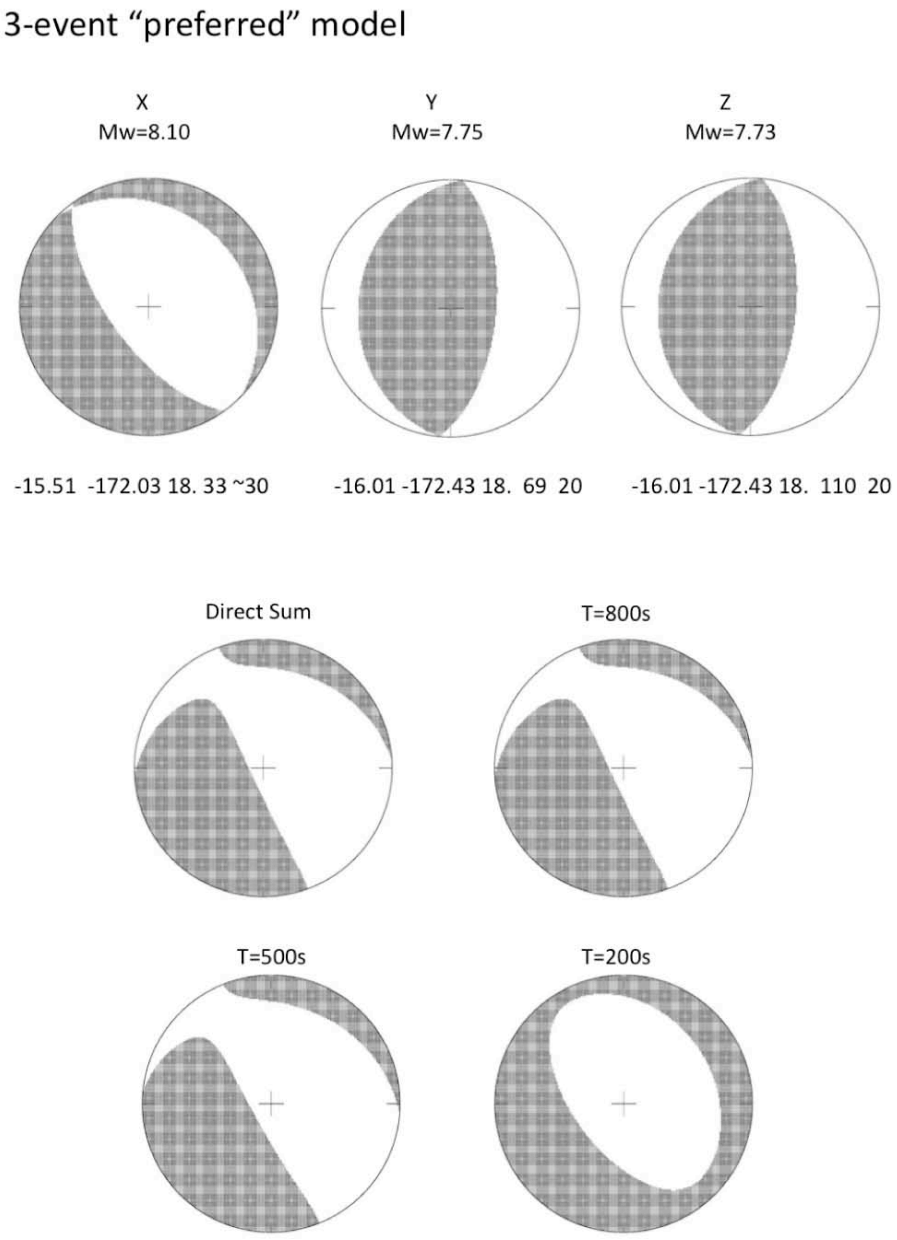

Figure S16. The main events of the 2009 Samoa-Tonga great earthquake sequence are modeled as a triplet, with the focal mechanisms, magnitudes, locations, depths and source function half durations indicated in the top row. The static, direct sum of the moment tensors is shown below, along with moment tensors for different period waves allowing for the time dependence of the source process. For the period range 200-500 s, the composite radiation is compatible with the W-phase solution.

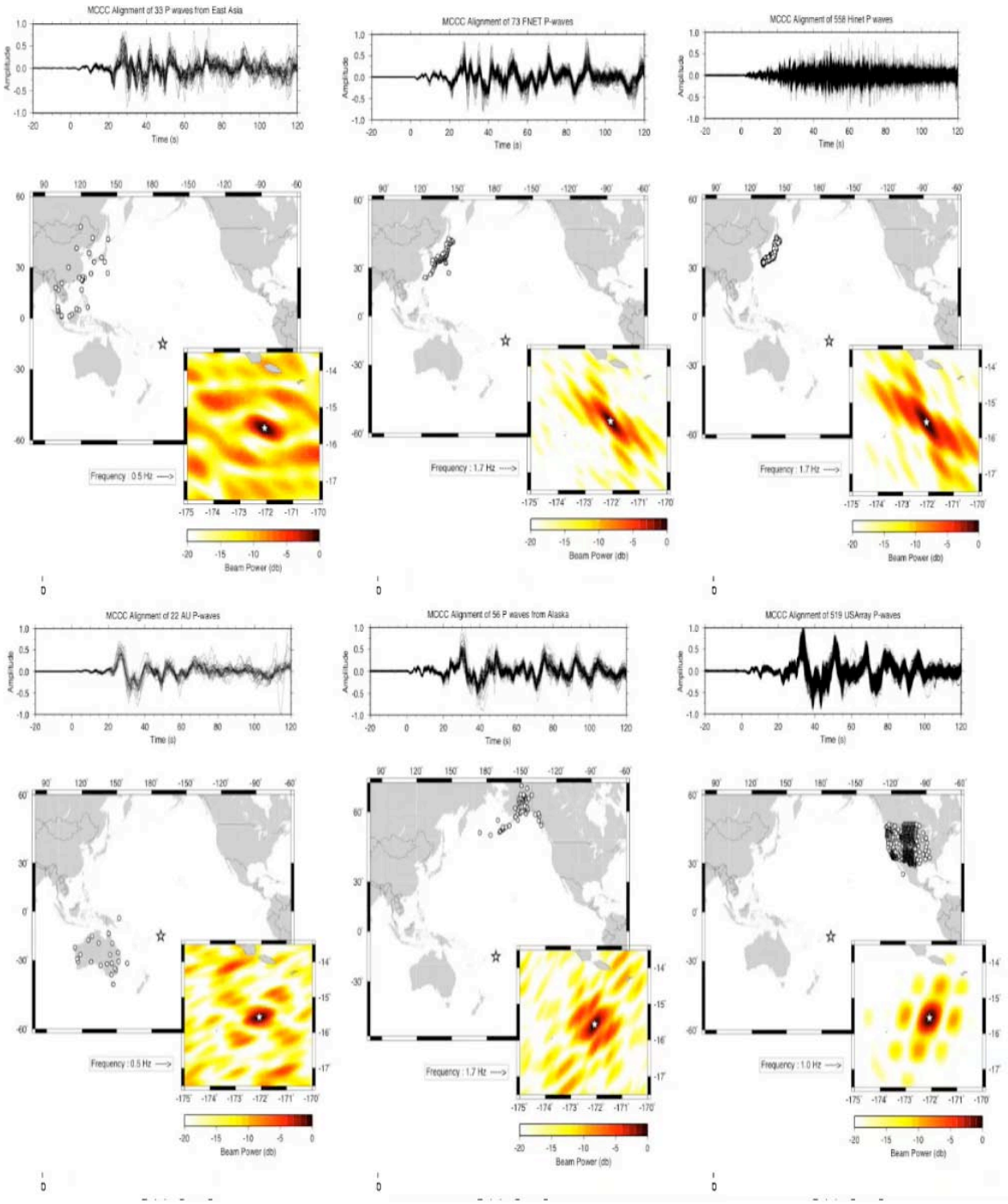

Supplementary Movie 1. Animation of P wave back-projections from 6 regional networks.

QuickTime Movie LAKRKH_Movie1.mov [H.264 Encoded QuckTime Movie; ~1.7MB].

http://es.ucsc.edu/~thorne/NATURE_Samoa/LAKRKH_Movie1.mov

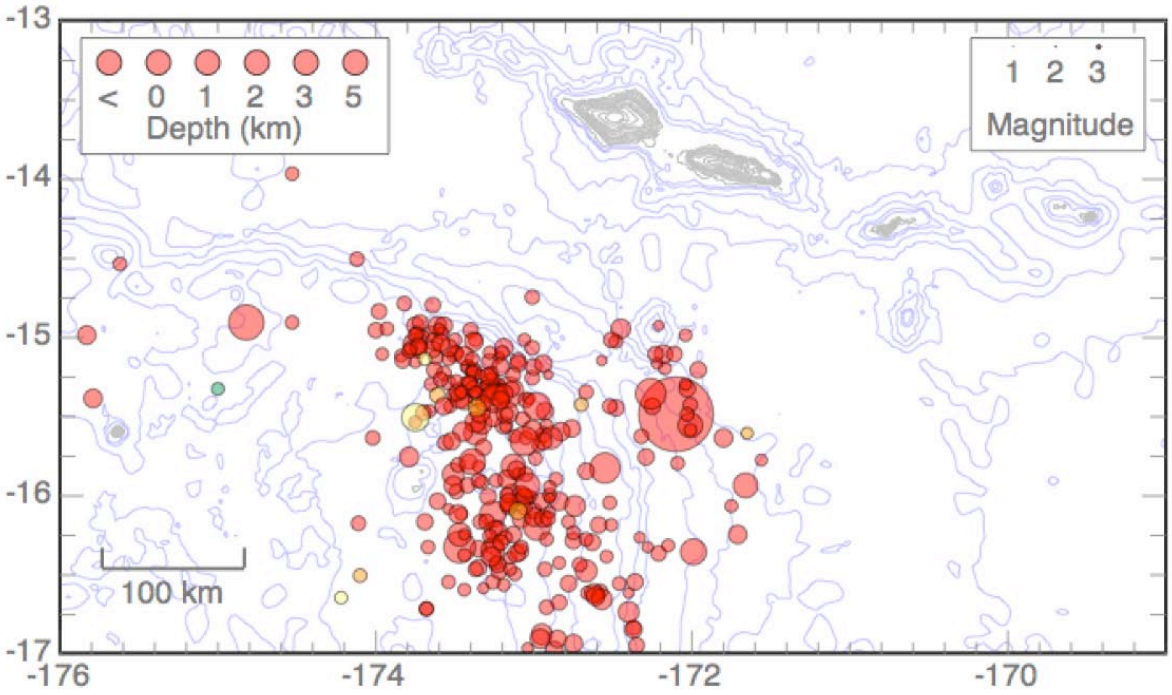

Supplementary Movie 2. Animation of the USGS located aftershock sequence.

QuickTime Movie LAKRKH_Movie2.mov [H.264 Encoded QuckTime Movie; ~1.2MB].

http://es.ucsc.edu/~thorne/NATURE_Samoa/LAKRKH_Movie2.mov